8

Effective Cloud Properties for Large-Scale Models

Robert F. Cahalan

8.1 Introduction

The large-scale terrestrial climate is well-known to be sensitive to small changes in the average albedo of the earth-atmosphere system. Sensitivity estimates vary, but typically a 10% decrease in global albedo, with all other quantities held fixed, increases the global mean equilibrium surface temperature by 5°C, similar to the warming since the last ice age, or that expected from a doubling of CO_2 (e.g., Cahalan and Wiscombe, 1993). Yet not only is the global albedo of 0.31 only known to $\approx 10\%$ accuracy[1] but current global climate models often do not predict the albedo in each gridbox from realistic cloud liquid water distributions; they normally tune the liquid until plane-parallel radiative computations produce what are believed to be typical observed albedos. The inability of global climate models to compute the

---

[1] Estimates of global albedo range from 0.30 to 0.33, or 3 out of 31 $\approx 10\%$, (e.g., Kiehl and Trenberth, 1997).

albedo is due to their inability to predict the microphysical and macrophysical properties of cloud liquid water within each gridbox, and their reliance on plane-parallel radiative codes. As Stephens (1985) has emphasized, the mean albedo of each gridbox depends not only on the mean properties of clouds within each box, but also upon the variability of the clouds, which involves not only the fractional area covered by clouds, but also the cloud structure itself. During recent years many climate models began to carry liquid water as a prognostic variable, e.g., Sundqvist et al. (1989) and Tiedtke (1996). It is important to treat cloud radiation and cloud hydrology consistently, which requires that cloud parameterizations become dependent on the fractal structure of clouds. Radiative properties of singular multifractal clouds have been previously studied (e.g., Cahalan, 1989; Cahalan and Snider, 1989; Lovejoy et al., 1990; Gabriel et al., 1990; Davis et al., 1990). Here we shall show how radiative properties of marine stratocumulus boundary-layer clouds, and specifically area-average albedo of these clouds, depend on their structure. The central role of this cloud type in maintaining the current climate was clarified and quantified in Ramanathan et al. (1989).

The dependence of average albedo on cloud structure has been found to be especially important in the case of marine stratocumulus, a major contributor to net cloud radiative forcing. Computations based on observations of California stratocumulus during the First International Satellite Cloud Climatology Project (ISCCP) Regional Experiment (FIRE) have shown that stratocumulus have significant fractal structure, and that this "within-cloud" structure can have a greater impact on average albedo than cloud fraction (Cahalan and Snider, 1989; Cahalan et al., 1994b,a). These studies employed a "bounded cascade" model to distribute the cloud liquid, defined in terms of two cascade parameters: f, the difference in cloud liquid fractions between two segments of the full cloudy domain being considered, and c, the difference of liquid fractions at the next smaller scale (within each segment) divided by f.[2] Parameters c and f are empirically adjusted to fit the scaling exponent of the power spectrum of liquid water path (W), $\beta(c) \approx 5/3$, and the standard deviation of $\log W$, $\sigma(f)$, respectively. In order to isolate the effects of horizontal liquid water variations on cloud albedo, it is convenient to assume that the usual microphysical parameters are homogeneous, as is the geometrical cloud thickness. In order to simplify comparison with plane-parallel clouds, the area-averaged vertical optical depth is kept fixed at each step of the cascade. The albedo bias is then found as an analytic function of the fractal parameter, f, as well as the mean vertical optical thickness, τ_v, and sun angle, θ_0. For the diurnal mean of the values observed in FIRE ($f \approx 0.5$, $\tau_v \approx 15$, and $\theta_0 \approx 60°$) the absolute bias is approximately 0.09, nearly 15% of the plane-parallel albedo of 0.69. Diurnal and seasonal variations of cloud albedo bias have been determined from observations during the Atlantic Stratocumulus Transition Experiment (ASTEX) and compared to the FIRE results (Cahalan et al., 1995).

---

[2] Bounded cascades were first introduced in Cahalan et al. (1990), and their scaling properties studied in Marshak et al. (1994). For a description of bounded cascades in terms of f and c, see the discussion following (8.2) below.

The goal of this chapter is to show how these results for the mean albedo of bounded cascade clouds, derived in the references cited above, may be applied to parameterizing the albedo of such clouds in terms of the plane-parallel albedo of a cloud having an "effective optical thickness" which is reduced from the mean thickness by a factor $\chi(f)$ which depends only on the fractal parameter f, or equivalently $\sigma(f)$, and not on the mean cloud properties. This "effective thickness approximation" (ETA) is a special case of the more general "independent pixel approximation" (IPA), sometimes referred to as the "independent column approximation" (ICA) especially for gridded climate models. The key assumption of any IPA (or ICA) type approximation is the neglect of horizontal photon transport (see Chap. 12). In addition, it depends only on 1-point cloud probability distributions, not on the spatial arrangement or correlations of individual cloud elements. On the other hand, knowledge of the *accuracy* of any IPA approximation depends on three-dimensional (3D) radiative transfer (i.e., with net horizontal fluxes) as well as on the spatial (typically fractal) cloud structure. In this chapter, though we compare the IPA/ICA with 3D radiative transfer as is done in other chapters, the primary purpose is to compare the IPA with the much simpler ETA. In particular, we use a simple fractal "bounded cascade" model to (1) motivate the ETA; and (2) determine the accuracy of the ETA by comparing it to the full IPA, using cloud parameters typical of marine stratocumulus. Moreover, some analytic results for bounded cascades are generalized and simplified in two appendices. In the "Further Readings" section at the end, we point the reader to simple alternatives to the ETA, each of which have particular advantages and points of view. We feel that each approximation is helpful insofar as it lends some insight into real clouds, which are far more complex than any of our mathematical idealizations, as anyone can discover who takes the opportunity to study the amazing variety of real cloud systems.

In the following, we first define some terms in Sect. 8.2. Then Sect. 8.3 shows that the IPA provides estimates of the plane-parallel albedo bias accurate to about 1% for bounded cascade clouds, and Sect. 8.4 applies the IPA to show that the total absolute bias reaches a maximum of about 0.10 during the morning hours, when the cloud fraction is nearly 100%. These two sections are primarily summaries of results from Cahalan et al. (1994b) and Cahalan et al. (1994a), although there a 1D cascade was employed, while a here a 2D cascade is applied. Section 8.5 gives the main result, that under certain commonly-observed conditions the albedo is approximately the plane-parallel albedo at a reduced "effective optical thickness" $\tau_{\mathrm{eff}} \equiv \chi\tau_{\mathrm{v}}$, where the reduction factor χ decreases with f, or equivalently $\sigma(f)$, approximately as $10^{-1.15\sigma^2}$ (see Fig. 8.5 and (8.B.12)), independently of the mean vertical optical depth, τ_{v}. The accuracy of this approximation is given as a function of both f and the mean thickness. The results are summarized and their limitations briefly discussed in Sect. 8.6. Appendix 8.A shows that all moments of a bounded cascade may be obtained by considering only the second moment as a function of the fractal parameter. This generalizes expressions for the second and third moments given in Cahalan et al. (1994a), and allows the lognormal behavior in the singular limit to be explicitly exhibited (see also Cahalan, 1994). Appendix 8.B gives expressions for $\chi(f)$

and $\sigma(f)$ as power series in f with coefficients depending on c, and evaluates the coefficients for the case of a $\beta(c) \approx 5/3$ wavenumber spectrum.

8.2 Definitions

Many general circulation models (GCMs) are now predicting mean cloud liquid water in each gridbox, not merely diagnosing it from other quantities. The cloud albedo could potentially also be accurately predicted, if cloud liquid could be accurately distributed within each gridbox. Efforts are underway to improve the treatment of cloud distributions in global models, so that simulated clouds can respond more realistically to climate change. The hope is that average cloud liquid in each gridbox will be accurately predicted, and that the resulting cloud albedo will be correctly computed from this, and other average cloud parameters. It is important to recognize, however, that *mean cloud parameters are insufficient* to compute the mean albedo. The mean albedo also depends, at a minimum, on the deviations of the liquid water from the mean, for instance, on the mean *and standard deviation* of the logarithm of the liquid water. We demonstrate this here and in the next using the bounded cascade model.

The schematic in Fig. 8.2 shows three approaches to distributing a prescribed amount of liquid water in a given vertical level of a GCM gridbox. In (a) it is uniform over the whole area, and thus the albedo may be computed from plane-parallel theory, and depends only on the *average* optical thickness, effective particle radius, and so on. In (b) the cloud is assumed to cover only a fraction of the area, is somewhat thicker in order to contain the same total liquid, but is still assumed to be uniform on that so-called "cloud fraction." In this case the mean albedo of the gridbox is assumed to equal the area-weighted average of a "cloud albedo" and a "clear-sky" albedo. Finally, in (c) the cloud covers the same cloud fraction as in (b), with the same mean parameters, but is assumed to have a non-uniform structure which depends on one or more "fractal parameters." The cloud fraction and the fractal parameters are assumed to depend on geographic region, season, and time of day.

As a measure of the impact of cloud fraction and fractal parameters on the average albedo, we define the "absolute plane-parallel albedo bias" ΔR_{pp}, as the mean albedo computed in case (a) minus that in case (c). This may be expressed symbolically as:

$$\Delta R_{pp} = R_{pp} - [A_c R_f + (1 - A_c)R_s], \qquad (8.1)$$

where R_{pp} is the plane-parallel reflectivity, R_f is the mean reflectivity of the fractal cloud, R_s is the mean clear-sky reflectivity, and the same total liquid water is used in all cases. The *relative* plane-parallel albedo bias is the absolute bias divided by R_{pp}. To avoid confusion, the absolute bias is always given as a fraction, while the relative bias is given in percent. Since the simple uniform cloud fraction model shown in Fig. 8.2b is currently widely employed, it is convenient to split the total plane-parallel bias into the difference between (a) and (b), plus the difference between (b) and (c). Symbolically:
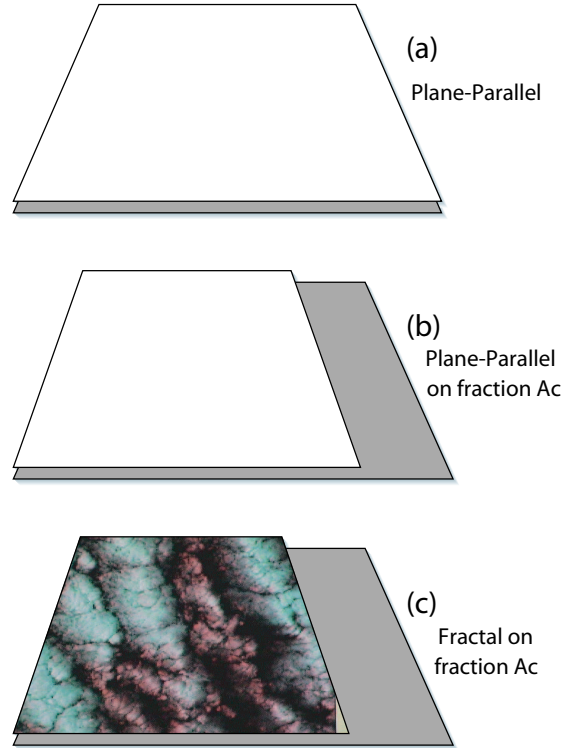
Fig. 8.1. Schematic showing three approaches to distributing the cloud liquid water in a GCM gridbox. In the top figure, the cloud has plane-parallel geometry, with cloud parameters such as vertical optical thickness, τ_v, uniform over the whole gridbox. In the middle figure, the parameters are uniform over a fraction A_c of the gridbox, with the same values as above, except that cloud vertical optical thickness increases to τ_v/A_c, thus preserving the total liquid, while the cloud thickness is zero on the remaining fraction $1 - A_c$. In the bottom figure one has a fractal distribution of cloud parameters over the fraction A_c, with the same mean values as in the middle, and an identical clear fraction $1 - A_c$.

$$
\begin{aligned}
\Delta R_{pp} = &\{R_{pp} - [A_c R_{pp} + (1 - A_c)R_s)\} \\
&+ \{[A_c R_{pp} + (1 - A_c)R_s] \\
&- [A_c R_f + (1 - A_c)R_s]\}.
\end{aligned}
\tag{8.2}
$$

The first difference represents the bias due only to the reduction in cloud fraction from unity to A_c, and the corresponding increase in thickness, with no change in the plane-parallel assumption; the second difference is the *additional* bias due only to the within-cloud fractal structure, where again the same total liquid is employed in all cases. This section and the following considers the case of overcast clouds, having $A_c = 1$, so that the total bias depends only on the fractal parameter. Then Sect. 8.4 considers the case in which both the cloud fraction and the fractal parameter follow the diurnal variations observed in California marine stratocumulus. As we shall see,

the $A_c = 1$ case produces the largest total bias, because of the sensitivity of the bias to the fractal structure, and the observed fact that in California stratocumulus the overcast cases have the greatest within-cloud variability.

In order to generate a bounded cascade cloud, we begin with a uniform cloud having a liquid water path of, e.g., $W = 100$ g/m^2, and corresponding vertical optical thickness of, e.g., $\tau_v = 15$ (assuming an effective drop radius of $r_e = 10\,\mu$m). We assume large but finite horizontal optical thicknesses in both horizontal directions, say $\tau_h = 1500$. This uniform distribution is then made non-uniform by a bounded multiplicative cascade process, in which the cloud is successively subdivided into smaller parts, and successively smaller fractions of liquid water are transferred among these parts, without changing the total.[3]

It is simplest to describe a one-dimensional (1D) bounded cascade, and we shall consider the simplest subdivision process: Divide the cloud in half along a north-south line. Flip a coin to select one half, and transfer a fraction, say $f_0 = f = 0.5$ from that half to the other one. The process is then iterated as follows: Each of the two halves is divided in half the same way, two coins are flipped to select one quarter from each of the two pairs, and a smaller fraction $f_1 = f \times c$, with say $c = 0.8$, so that $f_1 = 0.4$, is transferred from each chosen quarter to the other one. The resulting four quarters are in turn divided in half, four coins are flipped, and a fraction $f_2 = f_1 \times c = 0.32$ is transferred within the four pairs of eighths, and so on. The resulting distribution of liquid water path has a power spectrum behaving as $k^{-\beta}$, where $\beta \approx 5/3$ when $c = 2^{-1/3} \approx 0.8$, as observed (Cahalan and Snider, 1989), and an approximately lognormal probability distribution, with the standard deviation of $\log W$, $\sigma(f) \approx 0.39$ when $f = 0.5$, as is also observed (Cahalan et al. (1994a); see also Gage and Nastrom (1986) and Lilly (1989)).

A two-dimensional (2D) bounded cascade begins with the same initial cloud, which is then divided into quarters along both north-south and east-west lines, and liquid water fractions are then transferred among the quarters. One transfer method is as follows: The four quarters are divided into three pairs, aligned either north-south, east-west or diagonally, with equal probability for each of the three possible ways. One of the pairs is selected randomly, and a fraction $f_0 = f = 0.5$ is transferred within that pair, with either direction equally likely, while a fraction f_0' is transferred within the other pair. For simplicity we also take $f_0' = f$. The process is then repeated by quartering each quarter, transferring a fraction $f_1 = 0.8 \times f$, and so on. The set of optical depth values thus generated at steps 1, 2, 3, ..., N in the 2D cascade are identical to those generated at the same steps in the 1D cascade, except that each value appears twice in the first step, and 2^N times in the Nth step. The one-point probability distribution functions (the PDFs) of W and τ_v are identical in both 1D and 2D.

Table 8.1 summarizes the symbols and typical values of parameters in the bounded cascade cloud model. In addition to the bounded cascade, two additional assump-

---

[3] If the fractions were kept the same at each step, the resulting distribution would be singular, and the power spectrum would have more small-scale variability than is observed in marine stratocumulus clouds.

Table 8.1. Structural and optical parameters for bounded cascade cloud models.

Parameter	Symbol	Typical Value
single-scattering albedo	ϖ_0	1
asymmetry	g	0.85
liquid water path	W	100 g/m^2
liquid water path	r_e	10 μm^2
vertical optical thickness	τ_v	15
solar zenith angle	θ_0	60°
scaling parameter	c	0.794
spectral exponent	$\beta(c)$	5/3
variance parameter	f	0.5
reduction factor	$\chi(f,c)$	0.7
effective optical thickness	τ_{eff}	10

tions are being made here. One is that the effective droplet radius is uniformly equal to 10 μm, so that the vertical optical thickness of each part of the cloud is linear in the liquid water:

$$\tau_v = 0.15\,W \tag{8.3}$$

where W is expressed in g/m^2.[4]

Second, we employ the "independent pixel approximation" or IPA, which means that the reflectivity of each cloud pixel is assumed to depend only on its optical depth, $R = R(\tau)$, and not the optical depth of neighboring pixels. This is a strong assumption, and will be justified for the bounded model in the following section.

8.3 Independent Pixel Approximation

The grayscale map in Fig. 8.3a shows the reflectivity of 64×64 cloud cells as computed with a Monte Carlo method for a cloud generated by 6 cascade steps of a 2D bounded cascade with mean vertical optical thickness $\tau_v = 16$, $\theta_0 = 60°$, and fractal parameter $f = 0.5$. If there were no horizontal photon transport, the reflectivity of each of the $2^{12} = 4096$ cloud pixels would simply be determined by independent plane-parallel computations. The local differences between this "independent pixel approximation" (IPA) and the Monte Carlo reflectivities are shown by the grayscale map in Fig. 8.3b. The brighter areas of negative bias occur where the IPA underestimates the reflectivity of an optically thick region which lies on the sunward side of immediately adjacent thin regions and has an enhanced brightness due to photons escaping from those thin regions. Conversely, the darker positive regions occur where the IPA overestimates the brightness of a thin region which lies downstream of an

---

[4] The proportionality constant $\tau_v/W = 3/2\rho_w r_e$ in the limit of large size parameters in Mie scattering theory, and it equals 0.15 m^2/g if $r_e = 10\mu$m.

adjacent thick region.[5] These local errors in the IPA can be quite large, with magnitudes exceeding the plane-parallel bias of about 0.1 and in one area even exceeding 0.25. However, the horizontal average of the IPA bias is an order of magnitude smaller than the plane-parallel bias, because the positive and negative regions tend to approximately cancel in the area average.

The IPA has a long history of use in remote sensing, and was employed in a theoretical study by Ronnholm et al. (1980). But without any explicit model of the spatial structure, early studies could not examine the errors in the IPA. Here we find significant local errors in the IPA fluxes for the 2D bounded cascade, even though the model does not include geometrical cloud effects. The IPA is justified for the bounded cascade *only* for mesoscale-averaged fluxes, and even this simplification breaks down in the case of a singular cascade (Cahalan, 1989; Cahalan et al., 1994b).

When the sun is closer to the zenith than $\theta_0 \approx 60°$, the IPA errors tend to be of the same sign, but much smaller in magnitude. On the other hand, when the sun approaches the horizon, the reflectivity everywhere approaches unity, so all the biases are again smaller than at $\theta_0 \approx 60°$. As a result, the total IPA bias is maximum when the sun is near 60° (Cahalan et al., 1994a).

Since the horizontal average of the IPA errors is quite small, we may employ the IPA to estimate the average albedo, and compare it with the albedo of a uniform cloud having the same horizontal average optical depth. Thus we substitute this difference for the "plane-parallel albedo bias" defined in (8.1). It can be shown that the resulting plane-parallel bias is strictly positive as long as the reflection function is convex, unlike the IPA errors. (See Jensen (1906), also Sect. 12.3.) The plane-parallel albedo for the parameters used here is 0.69, while the average of Monte Carlo albedo (i.e., averaging over all pixels in a number of realizations such is the one in Fig. 8.3a) is 0.60. Thus the bias associated with using the area-average optical thickness is 0.09, which is 13% of the plane-parallel albedo.

As a result of the IPA , the mean albedo may be computed by simply transforming the optical depth of each pixel to reflectivity, and then averaging over all pixels. The results in the case of conservative scattering are shown in Fig. 8.3. The upper curve is the plane-parallel ($f = 0$) albedo as a function of mean liquid water path, and the lower curve is the fractal ($f = 0.5$) albedo. For a typical mean liquid water path of $W \approx 100$ g/m^2 ($\tau_v \approx 15$), Fig. 8.3 shows that the plane-parallel albedo of about 0.69 is reduced to about 0.60 by the fractal structure, implying a relative bias of approximately 15%. In order to obtain the correct albedo from a plane-parallel cloud, it is necessary to reduce the liquid water path, or optical thickness, by 30%. An explicit expression for this reduction is derived in Sect. 8.5.

Since in the IPA the reflectivity of a given pixel is a function of the local liquid water path, it may be expanded in a Taylor series as follows:

$$R(W) = R(\overline{W}) + (W - \overline{W})R'(\overline{W}) + \frac{1}{2}(W - \overline{W})^2 R''(\overline{W})$$
$$+ O((W - \overline{W})^3 R'''), \tag{8.4}$$

---

[5] Recall that the cloud has constant geometric thickness everywhere, so that the horizontal photon leakage is not simple geometrical shadowing. It occurs *within* the cloud.
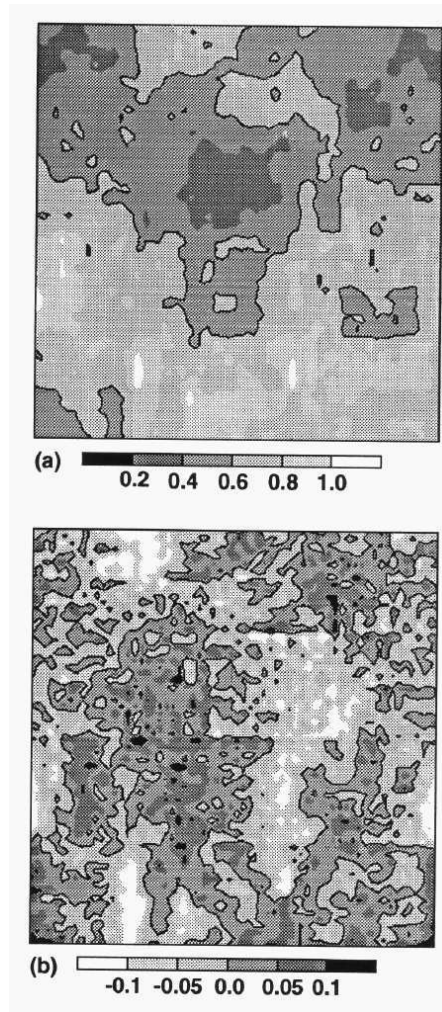
Fig. 8.2. (a) Contours of equal reflectance in a bounded cascade cloud with $A_c = 1$ and $f = 0.5$. Starting with a uniform cloud having mean vertical optical thickness $\bar{\tau} = \tau_v = 16$, 6 cascades were generated in each horizontal direction, giving $2^{12} = 4096$ uniform elements or "pixels". Reflectivities were computed by Monte Carlo with 10^7 photons. Microphysical properties are uniform, with single-scatter albedo $\varpi_0 = 1$ and asymmetry factor $g = 0.85$. The Henyey-Greenstein phase function was used, but essentially identical results are obtained from the fair weather cumulus phase function. The sun is $60°$ to the left of vertical. The black contour at 0.6 shows approximately where the reflectance equals the mean reflectance, with more reflective regions lighter, and less reflective regions darker. **(b)** Contours of equal "independent pixel bias" defined as the independent pixel reflectances (computed from the vertical optical thickness of each pixel) minus the Monte Carlo reflectances shown in (a). The average of these local algebraic biases is nearly an order of magnitude smaller than the "plane-parallel bias" namely the of the mean optical thickness minus the mean of the independent pixel reflectances, which is about 0.08.
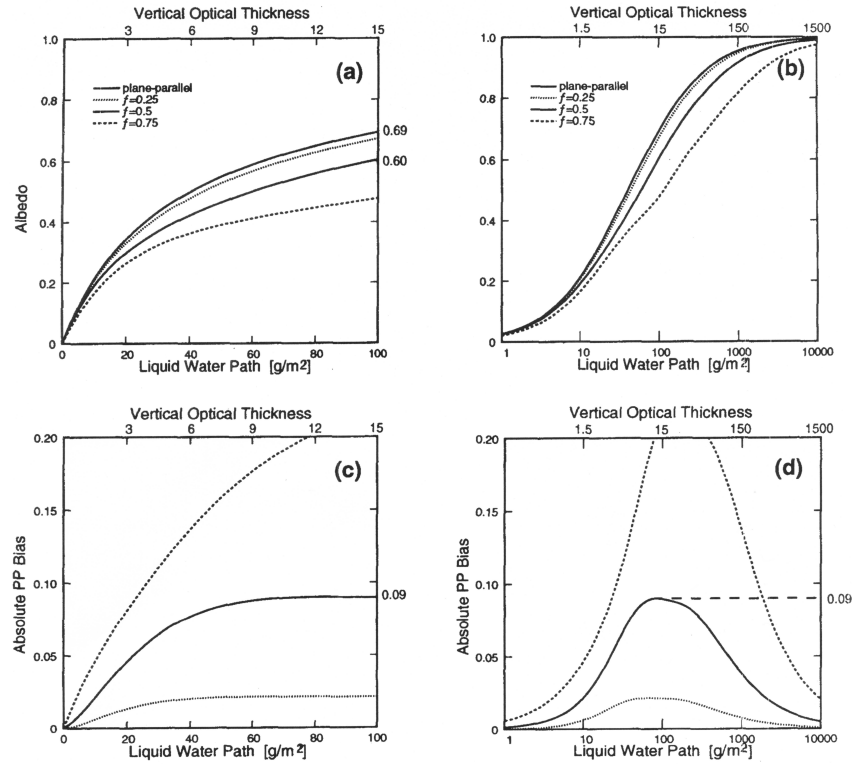
Fig. 8.3. (a) Albedo versus mean liquid water path [0–100 on lower axes], and vertical optical thickness [0–15 on upper axes], for the two approaches shown in Figs. 8.2a and 8.2c, where the fractal case is computed from the bounded model for $A_c = 1$ and $f = 0.25, 0.5, 0.75$, using the independent pixel approximation. **(b)** Same as (a) except plotted on log scales for liquid water [1–10,000 on lower axes], and optical thickness [0.15–1500 on upper axes]. **(c)** The "plane-parallel bias" obtained by subtracting the mean reflectance (the lower curves in (a)) from the reflectance of the mean (the upper curve). **(d)** Same as (c) except plotted on the same log scales used in (b). Note from (a) that for the typical $f = 0.5$, when $\tau_v = 15$ the bias is $0.69 - 0.60 = 0.09$, or $0.09/0.69 \approx 15\%$ of the plane-parallel albedo. Drawing a horizontal line in (a) at the mean reflectance 0.60 at $f = 0.5$ shows that this reflectance is that of a plane-parallel cloud having 30% less liquid water, or an optical thickness $\tau_{\mathrm{eff}} = 10$. The 30% reduction in cloud liquid corresponds to a value of the "reduction factor" of $\chi = 0.7$ (cf. (8.8) and (8.9)). Lack of significant curvature in (b) near $\tau_v = 15$, compared to the curves in (a), is the reason that an expansion in logs as in (8.6) is preferred over the ordinary Taylor expansion in (8.5).

where $\overline{W}$ is the average liquid water path, and $R'(\overline{W})$, $R''(\overline{W})$ and $R'''(\overline{W})$ are the successive derivatives of R with respect to W, evaluated at $\overline{W}$. (We have suppressed for simplicity the dependence of R on the solar zenith angle.) Averaging both sides of (8.4) eliminates the linear term on the right side, and we obtain

$$\overline{R(W)} = R(\overline{W}) + \frac{1}{2}\mu_2(f)R''(\overline{W}) + O(\mu_3 R'''), \qquad (8.5)$$

where μ_2 and μ_3 are the second and the third centered moments, respectively, of the one-point distribution of W generated by the bounded cascade. Subtracting (8.5) from $R(\overline{W})$ gives the plane-parallel albedo bias. The lowest-order term is positive, since the curvature R'' is negative (i.e., Fig. 8.3a shows convex graphs). This term overestimates the bias, while inclusion of the μ_3 term underestimates, and so on (see Cahalan et al., 1994a). Appendix 8.A shows that all the moments of the bounded model may be obtained from μ_2 (as a function of f), thus formally determining all the coefficients in the above expansion. In Sect. 8.5 we consider an alternative expansion about $\overline{\log(W)}$ (see Fig. 8.3b), which leads to a simple expression for the effective liquid water path and effective thickness. First, however, we briefly review the dependence of the bias on cloud fraction, A_c, to show that the overcast case, $A_c = 1$, assumed in the above discussion, is associated with the largest plane-parallel albedo bias during the diurnal cycle of California marine stratocumulus.

8.4 Diurnal Cycle

The total plane-parallel albedo bias has two contributions, as described in (8.2): (1) that due only to cloud fraction, which is given by the albedo for Fig. 8.2a minus that of Fig. 8.2b, and (2) that due to the fractal structure, given by the difference between Fig. 8.2b and Fig. 8.2c. The fractal structure contribution is largest when the liquid water variance is largest, which in the case of California marine stratocumulus occurs during the morning hours, when the cloud fraction is nearly 100%, as shown in Cahalan et al. (1994a). Although the cloud fraction contribution to the bias is larger in the afternoon, when the cloud fraction drops to 60%, this is more than offset by the decrease in the liquid water variance, which reduces both the fractal contribution and the total bias. The fact that the cloud variance is largest when the cloud cover is largest leads to the surprising result that plane-parallel estimates are most in error when the usual "cloud fraction" corrections vanish!

In Cahalan et al. (1994a) the diurnal cycle of the albedo bias was estimated indirectly, by first computing the diurnal cycle of f, determined from hourly values of the variance of $\log W$. Here we compute the bias directly from the time series of W, by performing a plane-parallel computation of reflectance for each observation, and then compositing the results hourly. The direct results agree qualitatively with the earlier indirect approach, and are shown in Fig. 8.4. Here the lower curve is the usual correction due only to cloud fraction, and vanishes when the fraction reaches 100% around 10 am. The middle curve is the additional correction due to the fractal distribution of the cloud liquid water. The upper curve is the total albedo bias. Note
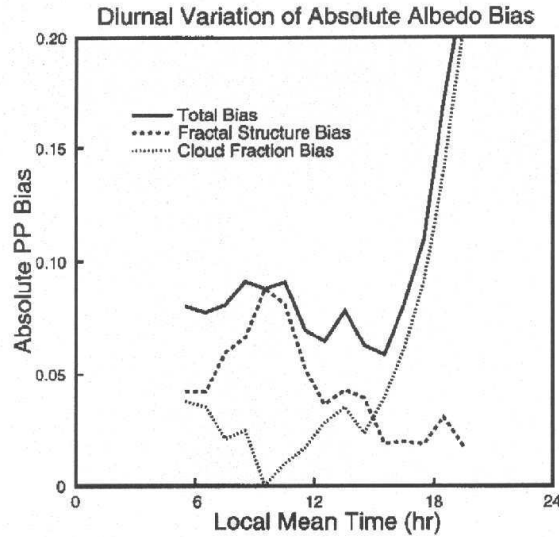
Fig. 8.4. Absolute plane-parallel albedo bias as a function of time-of-day for California marine stratocumulus, determined directly from microwave measurements of liquid water path during 18 days in June 1987, by computing an independent reflectivity from each measurement. The same computation using the bounded cascade model with diurnally varying f and A_c is given in Cahalan et al. (1994a), and is qualitatively similar. The upper solid curve is the total bias defined as in (8.1), while the dotted and dashed curves are the contributions due to cloud fraction and fractal structure, respectively, as defined in (8.2). Cloud fraction is defined as the fraction of values exceeding 10 g/m^2, and clear-sky albedo is taken to be zero.

that the cloud fraction correction is much smaller than the total, and is 180° out of phase with the total during most of the day (except when the sun is setting) when the total is dominated by the cloud fraction correction due to the neglect of the clear-sky albedo. The 0.09 albedo reduction needed when the clouds are overcast represents a major change in the average cloud albedo of 0.6.

8.5 Effective Optical Thickness

Since the largest albedo bias occurs for overcast cloudiness conditions, when $A_c = 1$, let us further consider that case, represented by the 15% increase in Fig. 8.3 of the albedo of a plane-parallel cloud over that of a fractal with the same total cloud water. As shown in Cahalan et al. (1994a), this bias may be estimated from a simple "effective thickness approximation" which is a lowest-order approximation to the bias determined from the IPA. To derive it, consider an expansion similar to (8.5), except now the local reflectance is considered as a function of the *logarithm* of the local liquid water path, $\log W$, and is expanded in a Taylor series about the mean, $\overline{\log W}$. Taking the mean of the result gives the mean cloud reflectivity as:

$$\overline{R(\log W)} = R(\overline{\log W}) + \frac{1}{2}M_2(f)R''(\overline{\log W}) + O(M_4 R''''), \qquad (8.6)$$

where M_2 is the variance of $\log W$, given in Appendix 8.B, and R'' is the second derivative of R with respect to $\log W$ evaluated at the mean of $\log W$. As a function of $\log W$, the conservative reflection function has an inflection point, where the slope stops increasing with $\log W$ and begins to decrease, and the curvature goes through zero, as seen in Fig. 8.3b. This typically occurs near $\overline{\log W}$. Thus the second term in the preceding equation is small, so that the mean reflectivity is approximately given by the reflectivity evaluated at $\overline{\log W}$. In the bounded cascade model, the mean of $\log W$ is given by

$$\overline{\log W} = \log W_{\text{eff}}, \qquad (8.7)$$

where

$$W_{\text{eff}} = \overline{W}\chi(f, c), \qquad (8.8)$$

and $\chi(f, c) < 1$ is the "reduction factor" given in (8.B), and is approximately 0.7 when $f = 0.5$ and $c = 0.8$, the appropriate values for typical cloud liquid water distributions (see below).

Combining (8.8) with (8.3), allows us to define the "effective optical thickness":

$$\tau_{\text{eff}} = \tau_{\text{v}}\chi(f, c), \qquad (8.9)$$

where τ_{v} is the mean vertical optical thickness. Taking only the first term in the expansion in (8.6), and using (8.3), it is clear that for a range of intermediate mean cloud thicknesses near the inflection point of the reflectivity, the mean albedo may be approximated by the plane-parallel albedo evaluated at the effective thickness, as follows:

$$\overline{R(\tau)} \approx R(\tau_{\text{eff}}), \qquad (8.10)$$

An estimate of the plane-parallel albedo bias may be obtained by subtracting (8.10) from the plane-parallel albedo, $R(\tau_{\text{v}})$. The relative error in the bias estimate derived from (8.10) is shown in Fig. 8.5 as a function of f and τ_{v}, for $c = 0.8$ and a solar zenith angle of $\theta_0 = 60°$, which is typical for stratocumulus. For the contours labeled ± 30, for example, the bias obtained from the simple effective thickness approximation should be multiplied by 1 ∓ 0.3. Since the bias itself is on the order of 0.1, this corresponds to corrections of $\approx \mp 0.03$. The correction is dominated by the M_2 term in (8.6), and thus changes sign near the inflection point of $R(\log W)$.

According to (8.9), the effective optical thickness depends on the fractal structure through χ, which is a known analytic function of fractal parameters f and c. The fractal parameter f is in turn adjusted to give the observed value of σ, also a known analytic function of f and c, while c is fixed by the exponent of the wavenumber spectrum. Thus τ_{eff} is parametrically determined as a function of σ by varying f. Details are given in Appendix 8.B, and results are shown in Fig. 8.5 for both $c = 2^{-1/3} \approx 0.8$ needed to give a $\beta = 5/3$ wavenumber spectrum, and for the singular limit $c \to 1$, for which χ is a simple exponential given in (8.B.12). The point labeled $f = 0.5$ in Fig. 8.5 corresponds to the diurnal average value of $\sigma = 0.39$, determined
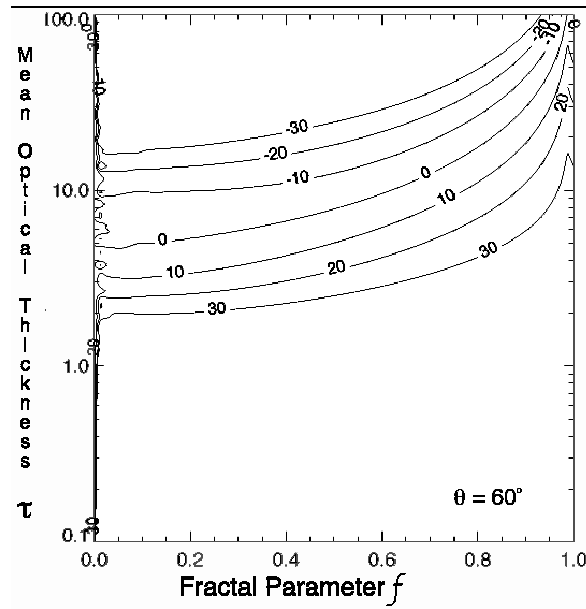
Fig. 8.5. Relative error in percent in the plane-parallel bias when the actual albedo is approximated by the plane-parallel albedo at a reduced "effective thickness" as a function of mean optical thickness τ_v and fractal parameter f. If the effective thickness gives an absolute bias of 0.10 near the –20 contour, for example, then the actual bias should be increased 20%, to 0.12, and similarly an estimate of 0.10 near the +20 contour should be decreased to 0.09. These same corrections can also be applied to the relative bias.

from the stratocumulus observations discussed in Sect. 8.4. In this case $\chi \approx 0.7$, so for example when $\tau = 15$ we have $\tau_{\text{eff}} \approx 10$, and $\overline{R} \approx 0.6$.

Harshvardhan and Randall (1985) found that the global average cloud liquid must be reduced by a factor of approximately 0.3 in order to obtain the correct global albedo. To obtain this value of the reduction factor, $\chi = 0.3$, for the bounded cascade model requires an increase in the fractal parameter to $f = 0.8$, and an increase in the standard deviation to $\sigma = 0.7$, as seen in Fig. 8.5. This in turn increases the plane-parallel albedo bias by a factor of 5. The fact that a much larger bias is found on a global basis is presumably due to the much wider variation in cloudiness over the globe, as compared to the relatively benign variation in marine stratocumulus. Davis et al. (1990) considered a related quantity, the "packing factor" the inverse of the reduction factor, and studied the thick cloud limit in a singular model, for which $\chi \rightarrow 0$, and the packing factor diverges. A similar singular model was studied in Cahalan (1989). The bounded model considered here is a relatively conservative extension of the plane-parallel idealization. More radical, and perhaps singular, models may be needed to better represent radiative processes in deep convective cloud systems.
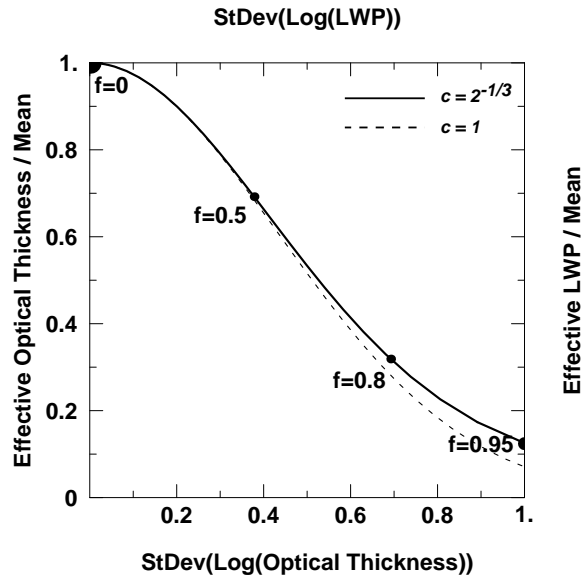
StDev(Log(LWP))

Fig. 8.6. Plot of χ, the reduction factor, versus σ, the standard deviation of $\log W$). Both the horizontal and vertical scales are independent of the number of cascade steps, and apply to either W or τ because of the simple linear relation expressed in (8.3). The solid curve is for the bounded model with $c \approx 0.8$, while the dashed curve is the singular limit given by the simple expression in (8.B.12). Labeled points apply only to the upper curve. The value of σ derived from observations of California marine stratocumulus is 0.39, corresponding to $\chi \approx 0.7$, which occurs at $f = 0.5$. (This is the diurnal mean in the summer, when f varies from about 0.6 in the morning to 0.3 in the afternoon.) The global reduction factor $\chi \approx 1/3$ discussed by Harshvardhan and Randall (1985) occurs at $f = 0.8$, and requires a global value of $\sigma \approx 0.7$.

8.6 Conclusions

A number of results on the mesoscale-average albedo of marine stratocumulus clouds, known to be a major contributor to cloud radiative forcing, have been reviewed in this chapter. A fractal cloud model which reproduces the observed power spectrum and low-order moments of the liquid water distribution in these clouds was studied by both 3D Monte Carlo and analytic methods. Local horizontal fluxes were determined from a 2D bounded cascade in Sect. 8.3, showing that errors in estimates of such fluxes by the "independent pixel approximation" or IPA can be large in some regions, though still producing an area-averaged reflectivity accurate to about 1%. Section 8.4 discusses the diurnal cycle of the variability of marine stratocumulus, showing the plane-parallel biases are largest when cloud fraction is near 100%.

The results suggest a way of parameterizing the impact of such cloud variability on the large-scale albedo in terms of an "effective" liquid water path, W_{eff} (or, equivalently, an "effective" optical thickness, τ_{eff}), smaller than the mean by a factor which depends on the fractal cloud structure. Section 8.5 determined the accuracy of this

"effective thickness approximation" or ETA, as a function of the fractal parameter f and the mean liquid water path $\overline{W}$ (or equivalently the mean optical thickness τ_v). The ratio of $\chi = W_{eff}/\overline{W}$ (or $\tau = \tau_{eff}/\tau_v$) was determined as an analytic function of the fractal parameters, and as a parametric function of σ, the standard deviation of $\log W$ (or $\log \tau$), which may be estimated from observations.

For marine stratocumulus, we find $\sigma \approx 0.4$ and $\chi \approx 0.7$ giving a mean albedo approximately equal to that of a plane-parallel cloud having 30% less liquid water, or 15% less than the plane-parallel albedo of a cloud with the same liquid water amount. A surprising result is that the plane-parallel albedo requires the largest adjustment when the cloud fraction is nearly 100%, since that is when the largest variability is observed. Thus the largest correction occurs when the usual cloud fraction correction is small.

The bounded cascade model studied here represents a relatively conservative extension to plane-parallel clouds, since the cloud height and base are fixed. We also keep the microphysics uniform. Yet even this conservative model shows that the variability of liquid water in marine stratocumulus can have a larger impact on the mesoscale average albedo than the usual cloud fraction corrections. For cloud types not confined to a single vertical layer, such as those found in deep convective regions, geometrical fractal properties neglected here may also impact large-scale radiative properties, and may well require more radical departures from conventional plane-parallel ideas. Fractal models for various surface types, including topography, vegetation and sea ice, need to be combined with cloud models in order to fully understand effects of inhomogeneity on atmospheric radiative transfer (see, e.g., Rozwadowska and Cahalan, 2002). Further study of the structure and radiation of real clouds and surfaces in their full complexity will be needed in order to understand how Earth's climate is being regulated, and in order to consistently quantify the role played by Earth's cloud systems on the energy and hydrological cycles.

Appendices

8.A Rescaling f Generates W Moments

Here we derive expressions for the moments of a bounded cascade, as a function of the cascade parameters f and c. We show that the moments may all be obtained from the second moment considered as a function of f, by rescaling the values of f. We then consider the singular limit $c \rightarrow 1$, and show that all moments approach those of a lognormal.

It is convenient to first define two sets of nth-order polynomials:

$$P_n(x) \equiv \frac{(1 + \sqrt{x})^{2n} + (1 - \sqrt{x})^{2n}}{2} = \sum_{m=0}^{n} \binom{2n}{2m} x^m, \qquad (8.A.1)$$

and

$$Q_n(x) \equiv \frac{(1+\sqrt{x})^{2n+1} + (1-\sqrt{x})^{2n+1}}{2} = \sum_{m=0}^{n} \binom{2n+1}{2m} x^m. \quad (8.A.2)$$

For example, the first four are given by:

n	$P_n(x)$	$Q_n(x)$	
1	$1+x$	$1+3x$	
2	$1+6x+x^2$	$1+10x+5x^2$	(8.A.3)
3	$1+15x+15x^2+x^3$	$1+21x+35x^2+7x^3$	
4	$1+28x+70x^2+28x^3+x^4$	$1+36x+126x^2+84x^3+9x^4$	

Values of bounded cascade have the form

$$W = \prod_{k=0}^{\infty} \left(1 \pm f\, c^k\right), \quad (8.A.4)$$

where $f, c \in (0,1]$. After averaging over $\pm$, the moments of W depend only on $a = f^2$ and $s = c^2$, and can be written in terms of the above polynomials in the form:

$$\mu_{2n}(a,s) = \prod_{k=0}^{\infty} P_n\left(as^k\right), \quad (8.A.5)$$

and

$$\mu_{2n+1}(a,s) = \prod_{k=0}^{\infty} Q_n\left(as^k\right). \quad (8.A.6)$$

For example, when $n = 1$,

$$\mu_2(a,s) = \prod_{k=0}^{\infty} \left(1+as^k\right) = 1 + \sum_{m=1}^{\infty} \left(\frac{s^{m(m+1)/2}}{\prod_{k=1}^{m}(1-s^k)}\right) a^m, \quad (8.A.7)$$

and

$$\mu_3(a,s) = \prod_{k=0}^{\infty} \left(1+3as^k\right) = \mu_2(3a,s). \quad (8.A.8)$$

The last expression for μ_2 in (8.A.7) was originally derived by Euler, as discussed by Hardy and Wright (1979), page 280. Taking the limit $s \to 1$, we can use the fact that

$$\lim_{s\to1} \frac{1-s^k}{1-s} = k$$

to show that

$$\lim_{s\to1} \left(\frac{\mu_2}{\exp(\frac{a}{1-s})}\right) = 1, \quad (8.A.9)$$

which implies an essential singularity in μ_2. The third moment is also singular, since

$$\lim_{s \to 1} \left(\frac{\mu_3}{(\mu_2)^3} \right) = 1. \tag{8.A.10}$$

We now generalize (8.A.8) and (8.A.10) to the remaining moments. By application of Sturm's theorem on polynomial roots localization, it can be shown that the roots of P_n, Q_n all lie on the negative real axis, so that we may write:

$$P_n(x) = \prod_{i=1}^{n} \left(1 + R_i{}^{(n)} x \right), \tag{8.A.11}$$

and

$$Q_n(x) = \prod_{i=1}^{n} \left(1 + \tilde{R}_i^{(n)} x \right) \tag{8.A.12}$$

where the $R^{(n)}, \tilde{R}^{(n)}$ are sets of positive real numbers with n elements. The first four sets are:

n	$R^{(n)}$	$\tilde{R}^{(n)}$	
1	1	3	
2	$3 - \sqrt{8},\ 3 + \sqrt{8}$	$5 - \sqrt{20},\ 5 + \sqrt{20}$	(8.A.13)
3	$7 - \sqrt{48},\ 1,\ 7 + \sqrt{48}$	$0.232,\ 1.572,\ 19.196$	
4	$0.040,\ 0.446,\ 2.240,\ 25.274$	$0.132,\ 0.704,\ 3,\ 32.163$	

Moments of order $2n$ and $2n + 1$ thus factor into n products:

$$\mu_{2n}(a, s) = \prod_{i=1}^{n} \mu_2 \left(R_i{}^{(n)} a, s \right), \tag{8.A.14}$$

and

$$\mu_{2n+1}(a, s) = \prod_{i=1}^{n} \mu_2 \left(\tilde{R}_i^{(n)} a, s \right), \tag{8.A.15}$$

so that all moments are determined by products of the second moment evaluated at various rescaled values of the fractal parameter $a = f^2$.

Combining (8.A.9) and (8.A.14), we find that in the singular limit,

$$\lim_{s \to 1} \left(\frac{\mu_{2n}}{(\mu_2)^{\sum_{i=1}^{n} R_i{}^{(n)}}} \right) = 1, \tag{8.A.16}$$

with a similar expression for the odd moments with $R_i \to \tilde{R}_i$. The sum of the roots can be shown to equal the coefficient of the linear term in (8.A.1), so that:

$$\sum_{i=1}^{n} R_i{}^{(n)} = 2n(2n - 1)/2, \tag{8.A.17}$$

and similarly for $\tilde{R}_i$. The limits for the even and odd moments can then be combined to yield:

$$\lim_{s \to 1} \left(\frac{\mu_n}{(\mu_2)^{n(n-1)/2}} \right) = 1 \,, \qquad (8.A.18)$$

consistent with the behavior of moments of a lognormal.

Summary. By considering the roots of P_n, Q_n in (8.A.11)–(8.A.12), we have seen in this Appendix that

1. all the moments are explicitly determined by the second moment evaluated at rescaled values of f, cf. (8.A.14) and (8.A.15); and
2. that the moments progress in the same ratios as for a lognormal distribution.

Note that this second fact does *not* imply that the pdf is lognormal, since a lognormal is *not* uniquely determined by its moments, though it is determined by the *moments of the logarithm*, which are discussed in Appendix 8.B. However, having the same ratios as a lognormal does show that the higher moments diverge in the same way as a lognormal when $s = c^2 \to 1$, each with an essential singularity, just like the variance in (8.A.9), diverging like $\exp[a/(1-s)]$.

8.B Reduction Factor and Variance of $\log W$

Here we derive simple polynomial approximations for the reduction factor and the standard deviation of $\log W$, or equivalently $\log \tau$, as a function of the fractal parameter f with coefficients depending on c. For $c = 2^{-1/3}$ (i.e., for –5/3 wavenumber spectral exponent) these are well approximated by rational functions of f accurate for $f < 0.9$. Also, we show that the reduction factor is approximately given by $\chi \approx \exp^{-\sigma^2/2}$, and insensitive to c as seen in Fig. 8.5.

The "effective" optical thickness defined in Sect. 8.5 is based on the following result for the liquid water path W:

$$\overline{\log W} = \log \left(\overline{W} \, \chi(f, c) \right), \qquad (8.B.2)$$

where the overbar signifies an area and ensemble average, and where the "reduction factor" is given by

$$\chi(f, c) = \left(\prod_{n=0}^{\infty} \left(1 - f^2 c^{2n} \right) \right)^{1/2}. \qquad (8.B.3)$$

Here f varies diurnally, as discussed in Sec. 8.4, but c is assumed constant, given by $c = 2^{-1/3}$, or

$$c^2 = 0.630, \qquad (8.B.4)$$

as required for a $k^{-5/3}$ wavenumber spectrum. Equations (8.B.2) and (8.B.3) were derived in Cahalan et al. (1994a) assuming the statistical distribution generated by the bounded cascade model. The reduction factor may also be expressed as

$$\chi(f, c) = 10^{-\Delta(f,c)}, \qquad (8.B.5)$$

where

$$\Delta(f,c) \equiv \log \overline{W} - \overline{\log W}, \tag{8.B.6}$$

A polynomial expression for Δ is obtained by taking $\log$ of (8.B.3), changing to base e by multiplying by $\log e$, and expanding in a power series in f, leading to

$$\Delta(f,c) = \frac{\log e}{2} \frac{f^2}{1-c^2}\left(1 + \frac{f^2}{1+c^2} + O\left(f^4\right)\right) \tag{8.B.7}$$

For the value of c^2 given in (8.B.4), a better fit than (8.B.7) is given by the rational approximant:

$$\Delta(f) = 0.594\, f^2 \left(\frac{1 - 0.485 f^2}{1 - 0.739\, f^2}\right), \tag{8.B.8}$$

which is accurate to 1% as long as $f < 0.9$.

The second moment of $\log W$ was derived in Cahalan et al. (1994a), and is given by

$$M_2(f) = \sum_{k=1}^{\infty}\left(\frac{1}{2}\log\left(\frac{1+fc^k}{1-fc^k}\right)\right)^2 \tag{8.B.9}$$

If we take the square root of (8.B.9), and expand the result in powers of f, we obtain the standard deviation of $\log W$ in the form:

$$\sigma(f,c) = \frac{f \log e}{\sqrt{1-c^2}}\left(1 + \frac{1}{3}\frac{f^2}{1+c^2} + O\left(f^4\right)\right). \tag{8.B.10}$$

The first term here agrees with the standard deviation obtained by taking the square root of the exponent of μ_2 in the singular limit in (8.A.9). For the value of c^2 in (8.B.4) a better fit is given by the approximant:

$$\sigma(f) = 0.718\, f \left(\frac{1 - 0.556\, f^2}{1 - 0.729\, f^2}\right). \tag{8.B.11}$$

which is accurate to 1% as long as $f < 0.9$.

Solving for f in (8.B.10), and substituting the result in (8.B.7) allows us to write (8.B.5) to lowest order as:

$$\chi(\sigma) = 10^{-\sigma^2/2\log e} \approx 10^{-1.15\,\sigma^2}. \tag{8.B.12}$$

The leading term in the exponent in (8.B.12) is independent of c, and the correction terms are of order σ^4, and quite small as long as $\sigma < 0.8$. The insensitivity to c is verified in Fig. 8.5.

References

Cahalan, R.F. (1989). Overview of fractal clouds. In *Advances in Remote Sensing*. A. Deepak Publishing, Hampton, VA, 371–388.

Cahalan, R.F. (1994). Bounded cascade clouds: Albedo and effective thickness. *Nonlinear Proc. Geophys.*, **1**, 156–167.

Cahalan, R.F., M. Nestler, W. Ridgway, W.J. Wiscombe and T. Bell (1990). Marine stratocumulus spatial structure. In *Proceedings of the Fourth International Conference on Statistical Climatology*, New Zealand Meteorological Service, Wellington, N.Z., J. Samson (ed.). 28–32.

Cahalan, R.F., W. Ridgway, W.J. Wiscombe, T.L. Bell and J.B. Snider (1994a). The albedo of fractal stratocumulus clouds. *J. Atmos. Sci.*, **51**, 2434–2455.

Cahalan, R.F., W. Ridgway, W.J. Wiscombe, S. Gollmer and Harshvardhan (1994b). Independent pixel and Monte Carlo estimates of stratocumulus albedo. *J. Atmos. Sci.*, **51**, 3776–3790.

Cahalan, R.F., D. Silberstein and J. Snider (1995). Liquid water path and plane-parallel albedo bias during ASTEX. *J. Atmos. Sci.*, **52**, 3002–3012.

Cahalan, R.F. and J.B. Snider (1989). Marine stratocumulus structure during FIRE. *Remote Sens. Environ.*, **28**, 95–107.

Cahalan, R.F. and W.J. Wiscombe (1993). Impact of cloud structure on climate. In *Current Problems in Atmospheric Radiation*. A. Deepak Publishing, Hampton, VA, 120–124.

Davis, A., P.M. Gabriel, S.M. Lovejoy, D. Schertzer and G.L. Austin (1990). Discrete angle radiative transfer III: Numerical results and meteorological applications. *J. Geophys. Res.*, **95**, 11,729–11,742.

Gabriel, P.M., S.M. Lovejoy, A. Davis, D. Schertzer and G.L. Austin (1990). Discrete angle radiative transfer II: Renormalization approach for homogeneous and fractal clouds. *J. Geophys. Res.*, **95**, 11,717–11,728.

Gage, K. and D. Nastrom (1986). Atmospheric wavenumber spectra of wind and temperature observed by comercial aircraft during GASP. *J. Atmos. Sci.*, **43**, 729–740.

Hardy, G.H. and E.M. Wright (1979). *An Introduction to the Theory of Numbers*. Oxford University Press, Oxford, UK.

Harshvardhan and D. Randall (1985). Comments on "The parameterization of radiation for numerical weather prediction and climate models". *Mon. Wea. Rev.*, **113**, 1832–1833.

Jensen, J.L.W.V. (1906). Sur les fonctions convexes et les inégalitiés entre les valeurs moyennes. *Acta Math.*, **30**, 175–193.

Kiehl, J.T. and K.E. Trenberth (1997). Earth's annual global mean energy budget. *Bull. Amer. Meteor. Soc.*, **78**, 197–208.

Lilly, D.K. (1989). Two-dimensional turbulence generated by energy sources at two scales. *J. Atmos. Sci.*, **46**, 2026–2030.

Lovejoy, S., A. Davis, P. Gabriel, D. Schertzer and G. Austin (1990). Discrete angle radiative transfer I: Scaling and similarity, universality and diffusion. *J. Geophys. Res.*, **95**, 11,699–11,715.

Marshak, A., A. Davis, R.F. Cahalan and W.J. Wiscombe (1994). Bounded cascade models as non-stationary multifractals. *Phys. Rev. E*, **49**, 55–69.

Ramanathan, V., R.D. Cess, E.F. Harrison, P. Minnis, B.R. Barkstrom, E. Ahmad and D. Hartmann (1989). Cloud-radiative forcing and climate: Results from the Earth-radiation Budget Experiment. *Science*, **243**, 57–63.

Ronnholm, K., M.B. Baker and H. Harrison (1980). Radiation transfer through media with uncertain or random parameters. *J. Atmos. Sci.*, **37**, 1279–1290.

Rozwadowska, A. and R.F. Cahalan (2002). Plane-parallel biases computed from inhomogeneous clouds and sea ice. *J. Geophys. Res.*, **107**, 4384–4401.

Stephens, G.L. (1985). Reply (to Harshvardhan and Randall). *Mon. Wea. Rev.*, **113**, 1834–1835.

Sundqvist, H., E. Berge and J. E. Kristjansson (1989). Condensation and cloud parameterization studies with a mesoscale Numerical Weather Prediction model. *Mon. Wea. Rev.*, **117**, 1641–1657.

Tiedtke, M. (1996). An extension of cloud-radiation parameterization in the ECMWF model: The representation of subgridscale variations in optical depth. *Mon. Wea. Rev.*, **124**, 745–750.

Suggested Reading

1. For an early clear description of the cascading effect of dynamical processes on cloud structure, see:

Welander, P. (1955). General development of motion in a 2D ideal fluid. *Tellus,* **7**, 141–156.

A modern and popularized discussion of the evolution of cascades is in

Barabasi, A.-L. (2003). *Linked: The New Science of Networks.* 256 pp., Perseus Publishing, Boulder (Co).

For a useful general approach to treating clouds in large-scale models, see:

Tiedtke, M. (1993). Representation of clouds in large-scale models. *Mon. Wea. Rev.* **121**, 3040–3061.

―――――――――――――

2. There are many interesting alternatives to the "effective thickness approximation" (ETA). Listed here are a few that are particularly instructive. A "generalized ETA" is described in:

Szczap, F., H. Isaka, M. Saute, B. Guillemet and A. Iolthukhovski (2000). Effective radiative properties of bounded cascade non-absorbing clouds: Definition of the equivalent homogeneous cloud approximation. *J. Geophys. Res.,* **105**, 20617–20633.

A generalization of the IPA to account for sun angle effects is the "tilted IPA" or "TIPA" of:

Várnai, T. and Davies, R. (1999). Effects of cloud heterogeneities on shortwave radiation: comparison of cloud-top variability and internal heterogeneity. *J. Atmos. Sci.,* **56**, 4206–4224.

Especially useful in the context of the "two-stream approximation" often used in large-scale models is the "Gamma-weighted two-stream approximation" described for example in:

Barker, H.W. (1996). A parameterization for computing grid-averaged solar fluxes for inhomogeneous marine boundary layer clouds - Part 1, Methodology and homogeneous biases. *J. Atmos. Sci.,* **53**, 2289–2303.

Oreopoulos, L. and H.W. Barker (1999). Accounting for subgrid-scale cloud variability in a multi-layer 1D solar radiative transfer algorithm. *Q. J. R. Meteorol. Soc.,* **126**, 301–330.

An interesting approach to taking advantage of cloud scaling properties in parameterizing effective cloud properties is the "renormalization" method described in (see also Chap. 6):

Cairns, B., A.A. Lacis and B.E. Carlson (2000). Absorption within inhomogeneous clouds and its parameterization in general circulation models. *J. Atmos. Sci.* **57**, 700–714.

A model that treats a cloud distribution analogously to the drop distribution within a cloud is the "independent scattering cloudlets" model described in:

Petty, G.W. (2002). Area-average solar radiative transfer in three-dimensionally inhomogeneous clouds: the independently scattering cloudlets model. *J. Atmos. Sci.*, **59**, 2910–2929.

---

3. There are many generalizations of the simple bounded cascade. For example, see:

Gollmer, S., Harshvardhan, R.F. Cahalan and J.B. Snider (1995). Windowed and wavelet analysis of marine stratocumulus cloud inhomogeneity. *J. Atmos. Sci.* **52**, 3013–3030.

There are also a multiplicity of cloud structure models that can be compared to the bounded cascade. We list here a few that are appropriate for various cloud types and applications. A model helpful in understanding large-scale cloud statistics, especially in the storm tracks, is the "cloud dot" model given in the appendix of:

Cahalan, R.F., D.A. Short and G.R. North (1982). Cloud fluctuation statistics. *Mon. Wea. Rev.* **110**, 26–43.

Interesting cascades have been developed for other geophysical fields, such as rainfall and vegetation. See for example:

Waymire, E. and V.J. Gupta (1981). The mathematical structure of rainfall representations 1. A review of the stochastic rainfall models. *Water Resour. Res.,* **17**, 1261–1294.

As c approaches unity in the bounded cascade, we reach an "essential " singularity that prevents the analytic continuation of the cloud properties to the singular $c = 1$ case. The singular case can be treated directly, as it is the so-called "p-model" of

Meneveau, C. and K.R. Sreenivasan (1987). Simple multifractal cascade model for fully developed turbulence. *Phys. Rev. Lett.,* **59**, 1424–1427.

Singularities in unbounded cascades can be tamed by integration, for example (see also the volume's Appendix) in the "fractionally integrated" model of:

Schertzer, D. and S. Lovejoy (1987). Physical modeling and analysis of rain and clouds by anisotropic scaling multiplicative processes. *J. Geophys. Res.,* **92**, 9693–9714.

The above is not meant to be an exhaustive bibliography, which would take too many pages, but only to point the reader in some interesting directions that may be helpful in their own areas of interest. Simple models of complex structure share many common features, so that often qualitative behavior discovered in the context of one simple model such as the bounded cascade, or any other listed above, may have surprisingly broad applicability. A model has served its purpose well if it prompts the researcher to ask productive questions that lead to a better understanding.